nature communications



Article

https://doi.org/10.1038/s41467-025-56101-8

Sun-simulated-driven production of highpurity methanol from carbon dioxide

Received: 21 May 2024

Accepted: 7 January 2025

Published online: 20 January 2025

Check for updates

Jiqing Jiao [®] ^{1.6} ⊠, Yanbin Ma^{1,6}, Xiaoqian Han¹, Awu Ergu², Chao Zhang¹, Pingping Chen [®] ¹, Wei Liu [®] ³, Qiquan Luo [®] ², Zhaolin Shi¹, Han Xu¹, Chen Chen⁴, Yaguang Li [®] ⁵ ⊠ & Tongbu Lu [®] ¹ ⊠

 CO_2 conversion to CH_3OH under mild conditions is of particular interest yet rather challenging. Both electro- and thermo-catalytic CO_2 reduction to CH_3OH can only produce CH_3OH in low concentration (typically mixed with water), requiring energy-intensive purification processes. Here we design a sun-simulated-driven tandem catalytic system comprising CO_2 electroreduction to syngas, and further photothermal conversion into high-purity CH_3OH (volume fraction > 97%). We construct a self-supporting electrocatalyst featuring dual active sites of Ni single atoms and encapsulated CO_2 and an encapsulated CO_2 ratio of CO_2 via solar-powered CO_2 electroreduction. The generated syngas is subsequently fed into the photothermal module, which could produce high-purity CH_3OH under 1 sun-light irradiation, with a rate of CO_2 such produce CO_2 into high-purity CO_2 into high-purity CO_3 into high-purit

Methanol (CH₃OH) is an important chemical feedstock widely acknowledged as a clean energy source^{1,2}. The conventional method for methanol production requires complex steps for purification, which typically leads to intense greenhouse gas emissions and high energy consumption^{3–5}. In contrast, electrocatalytic CO₂ reduction reaction (CO₂RR)^{6–8} could be readily integrated with renewable electricity (such as solar power), and convert CO₂ into CH₃OH^{9–12}. Although many state-of-art CO₂-to-CH₃OH electrocatalysts with high selectivity have been reported^{1,13–17}, the production of CH₃OH via electrochemical CO₂RR still faces the bottlenecks of low conversion and low catalytic activity^{18–20}. Moreover, the CH₃OH thus produced is mixed with electrolytes, which needs additional energy-intensive purification processes downstream²¹.

Recently, Li et al. demonstrated the electrochemical production of $\rm H_2$ powered by solar energy, and the obtained $\rm H_2$ was used in

thermocatalytic CO₂ hydrogenation to produce CH₃OH. They developed a binary metal oxide ZnO–ZrO₂, and achieved a CH₃OH selectivity up to 86–91% under 5.0 MPa². Ozin et al. prepared black indium oxide for a photothermal catalytic system, and the CH₃OH selectivity reached 49.23% at high hydrogen concentrations²². However, the high chemical inertness of CO₂ typically puts stringent requirements on the reaction conditions of hydrogenation, and water is an inevitable product, which could hamper the catalytic activity and product selectivity, thus lowering the CO₂ conversion and the concentration of produced CH₃OH. In contrast, CO hydrogenation could give CH₃OH as the sole product, and thus represents an atom-economical route²³. For single-active-site catalysts for CO₂RR, the selectivity for CO and H₂ is dependent mainly on the applied potential. Their ratios in these produced syngas may vary during the CO₂RR process with different

¹MOE International Joint Laboratory of Materials Microstructure, Institute for New Energy Materials and Low Carbon Technologies, Analysis and Testing Center, School of Materials Science and Engineering, Tianjin University of Technology, Tianjin 300384, China. ²Institutes of Physical Science and Information Technology, Anhui University, Hefei 230601 Anhui, China. ³School of Chemistry, State Key Laboratory of Fine Chemicals, Frontier Science Center for Smart Materials, Dalian University of Technology, Dalian 116024, China. ⁴Engineering Research Center of Advanced Rare Earth Materials, Department of Chemistry, Tsinghua University, Beijing 100084, China. ⁵Research Center for Solar Driven Carbon Neutrality, Engineering Research Center of Zero-carbon Energy Buildings and Measurement Techniques, Ministry of Education, The College of Physics Science and Technology, Institute of Life Science and Green Development, Hebei University, Baoding 071002, China. ⁶These authors contributed equally: Jiqing Jiao, Yanbin Ma. ⋈ e-mail: jiaojiqing101@163.com; liyaguang@hbu.edu.cn; lutongbu@tjut.edu.cn

applied potentials. Atomic catalysts generally have high selectivities, but the overpotential is often large, and the activity still needs to be improved. In order to produce syngas with a constant H_2 :CO ratio over a wide potential window, the key is to make sure that each type of catalytic sites would have high selectivity for a specific product within a broad potential range. Therefore, it is relatively difficult to efficiently produce syngas with a constant H_2 :CO ratio over a broad potential range for previous reports^{24–26} (Supplementary Table 1).

Herein, we designed a sun-simulated-driven tandem catalysis scheme that integrates photovoltaics-powered electrochemical CO_2RR and photothermally powered CO hydrogenation, which could store solar energy in the form of high-purity CH_3OH (volume fraction >97%). Employing an in situ synthesis strategy, we constructed a self-supporting binary electrocatalyst featuring dual-active sites²⁷. Different from the conventional impregnation methods, Ni single atoms (Ni SAs)^{28,29} were in situ anchored during the growth of carbon nanotubes encapsulating Co nanoparticles (Co NPs)³⁰, resulting in a composite core-shell structure. The single Ni atoms on the nanotube surface have a NiN₃ coordination structure, and could give a Faradaic efficiency for CO (FE_{CO}) >90% over a broad potential range; the encapsulated CO NPs could catalyze water electrolysis for producing H_2 . The resulting dual-active catalyst, with its composition optimized, could produce syngas

with an almost constant H₂:CO ratio of -2 across a broad potential window from $-0.6\,V$ to $-1.0\,V$ (vs. RHE). Under $-0.8\,V$ (vs. RHE), the catalyst could run stably with the H₂:CO ratio kept at 2.0 ± 0.2 . The flow cell equipped with our catalyst was powered by a photovoltaic panel, and the produced syngas after purification was further fed into a downstream photothermal reactor powered by broad-spectrum solar irradiation, and converted into high-purity CH₃OH (CH₃OH production rate under 1 sun irradiation, 0.238 g $g_{cat}^{-1}\,h^{-1}$). Our work here demonstrates a feasible all-solar route for converting CO₂ into high-purity methanol.

Results

Sun-simulated-driven production of high-purity CH₃OH

As shown in Fig. 1a, the produced green syngas (CO + H_2) was fed into a lab-built TiC-based photothermal device and light source (Supplementary Figs. 1, 2)^{22,31} containing commercial CuZnAl catalyst for CH₃OH synthesis (Supplementary Fig. 3). The light absorption spectrum of the photothermal device covered a broad range for sunlight (Supplementary Fig. 4). The interior surface of the photothermal device could reach a temperature as high as 359 °C (Supplementary Fig. 5) under 1 kW m⁻² intensity of sunlight irradiation (1 sun). Under merely 0.2 sun irradiation, the CuZnAl catalyst in the photothermal

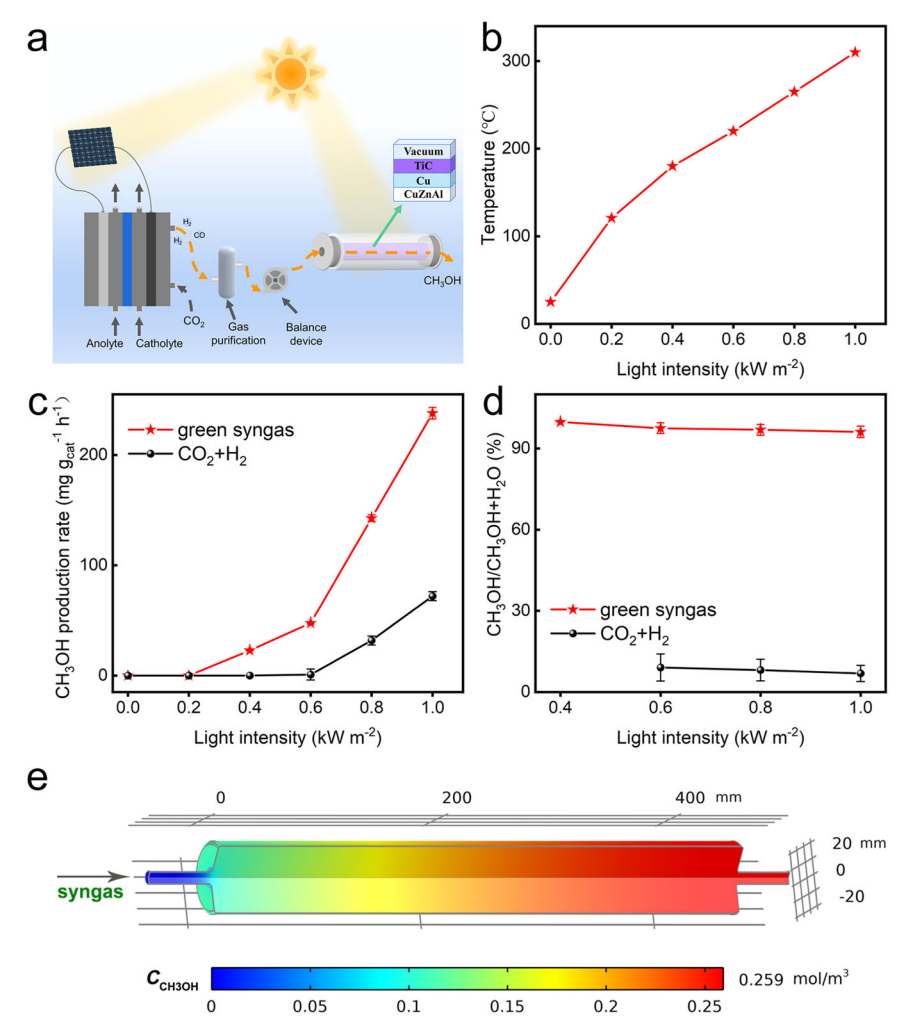


Fig. 1 | **Sun-simulated-driven production of high-purity CH₃OH from CO₂. a** Schematic illustration of the sun-simulated-driven tandem catalytic system that integrates photovoltaics-powered electrocatalysis and photothermal catalysis (under 4 MPa). **b** Temperatures of the catalyst in the photothermal device under different sunlight radiation intensities. **c** Comparison of CH₃OH production rates from different feed gases: green syngas, and CO₂ + H₂. **d** Volume fractions of

 $\text{CH}_3\text{OH}/(\text{CH}_3\text{OH} + \text{H}_2\text{O})$ produced from different feed gases (green syngas, and $\text{CO}_2 + \text{H}_2\text{)}$ under different sunlight radiation intensities. **e** Simulated concentration distribution of thermocatalytically generated CH_3OH vapor in the photothermal tube under 0.6 sun. Error bars represent the standard deviation of three independent measurements. Source data are provided as a Source Data file.

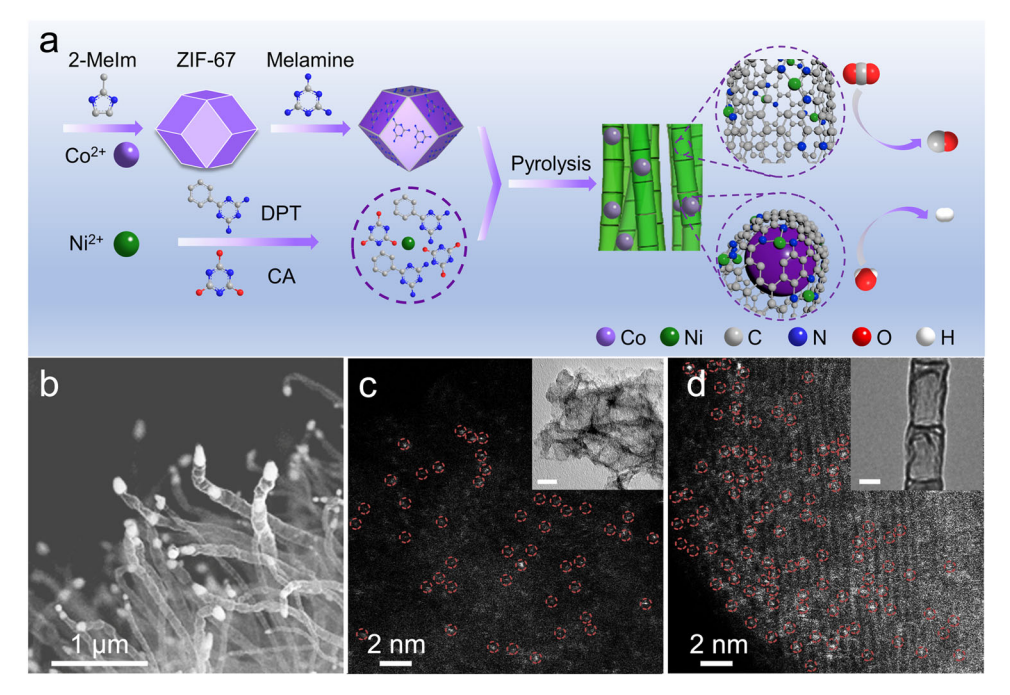


Fig. 2 | **Synthesis and characterizations of dual-active-site catalyst Ni SAs-Co NPs. a** Illustration of the synthesis procedure. **b** SEM image of Ni SAs-Co NPs. **c** HAADF-STEM image of Ni SAs. **d** HAADF-STEM image of Ni SAs-Co NPs (The

single-atomic sites are highlighted with red circles. Inset in (**c**, **d**): TEM image for corresponding catalyst. Scale bar: 20 nm).

device could reach 121 °C (Fig. 1b). With the sunlight intensity increased to 0.4 sun and 1 sun, the temperature of the catalyst was elevated to 180 and 310 °C, respectively, sufficient to initiate the methanol production. Under 0.2 sun irradiation, the photothermal system was barely functional (Fig. 1c); under 0.4 sun irradiation, the signal of CH₃OH emerged. Under 1 sun irradiation, the CH₃OH production rate was determined to be 238 mg g_{cat}⁻¹ h⁻¹; in contrast, the CH₃OH production rate from CO₂ and H₂ was only 72 mg $g_{cat}^{-1} h^{-1}$, and the signal of CH₃OH did not emerge until >0.6 sun. Furthermore, the liquid products from the photothermal device operating under 0.4 sun irradiation were almost pure methanol (Fig. 1d), indicating that the coupling of photovoltaics-powered electrocatalysis and photothermal catalysis can convert CO2 and H2O into pure methanol in terms of liquid product. The CO conversion rate in photothermal methanol production was achieved at 12.1% under 1 sun irradiation. The volume fraction of CH₃OH/(CH₃OH + H₂O) ranged from 97 to 100%, whereas the volume fraction corresponding to CO₂+H₂ feed gas was only 6-9%. As far as we know, this is the first report on CH₃OH production with an export content greater than 50%. In previous works, CO₂ and H₂ or water were used to generate CH₃OH under sunlight³². We further conducted finite-element analysis on the photothermal module working under 0.6 sun; the simulated concentration distribution of thermocatalytically generated CH₃OH vapor is displayed in Fig. 1e. A steady increase in CH₃OH vapor concentration could be noted along the flow path. The vapor thus produced could then be readily condensed downstream into high-purity CH₃OH.

Synthesis and structural characterization of dual-active-site catalyst

To obtain the high-purity methanol, syngas with a constant ratio is necessary. The CO and $\rm H_2$ should be produced via $\rm CO_2RR$ with stably balanced selectivities over a broad potential range so as to be compatible with the photovoltaic panel. Thus, a well-optimized catalyst is desired for the entire process. To this end, we designed and prepared a binary catalyst that features dual-active sites for stable production of CO and $\rm H_2$. Figure 2a illustrates the in situ preparation procedure for

the dual-active-site catalyst (denoted as Ni SAs-Co NPs) (see Methods section).

The morphology of the dual-active-site catalyst Ni SAs-Co NPs was examined via scanning electron microscopy (SEM). The carbon nanotubes (CNTs) therein with uniform diameters are shown in Fig. 2b. As shown in Supplementary Fig. 6, the bamboo-like CNTs, which were in situ grown under high temperature, can be distinguished from transmission electron microscopy (TEM) images. The small Co NPs are wrapped within the CNTs. The core-shell structure was characterized via high-resolution TEM (HRTEM). The surface of Co NPs is covered with carbon, which is due to the graphitization of amorphous carbon catalyzed by Co NPs at high temperatures. The lattice fringe spacing of Co NPs is 0.20 nm, corresponding to the (111) crystal plane of Co. The interplanar distance of 0.34 nm corresponds to the (002) plane of CNTs. The high-angle annular dark-field scanning transmission electron microscopy (HAADF-STEM) image (Fig. 2c) displayed abundant small bright spots (marked by red circles) on the CNTs, indicative of Ni single-atomic sites. A large number of Ni SAs are uniformly dispersed on the CNT walls (Fig. 2d). The X-ray diffraction (XRD) patterns for three samples are shown in Supplementary Fig. 7. The Ni SAs-Co NPs and Co NPs display three broad peaks at 45°, 52°, and 76°, corresponding to the (111), (200) and (220) planes of Co (PDF#15-0806)³³⁻³⁵, respectively, which are consistent with the HRTEM results. No diffraction peaks related to Ni NPs were detected, also indicative of their atomic dispersion. The actual loadings of Ni and Co were determined via inductively coupled plasma mass spectrometry (ICP-MS), as listed in Supplementary Table 2.

To probe the coordination environment and electronic structures of Ni atoms, we conducted synchrotron radiation-based X-ray absorption fine structure (XAFS) at the Ni K-edge for different samples³², the corresponding references, including Ni foil, NiO, and nickel phthalocyanine (NiPc). Figure 3a shows the X-ray absorption near-edge structure (XANES) profiles for Ni SAs and NiPc, and the edge positions are between those for Ni foil and NiO. The white-line peak intensities are significantly higher than that of Ni foil, indicating that the average valence state of Ni is between Ni^o and Ni^{II}.

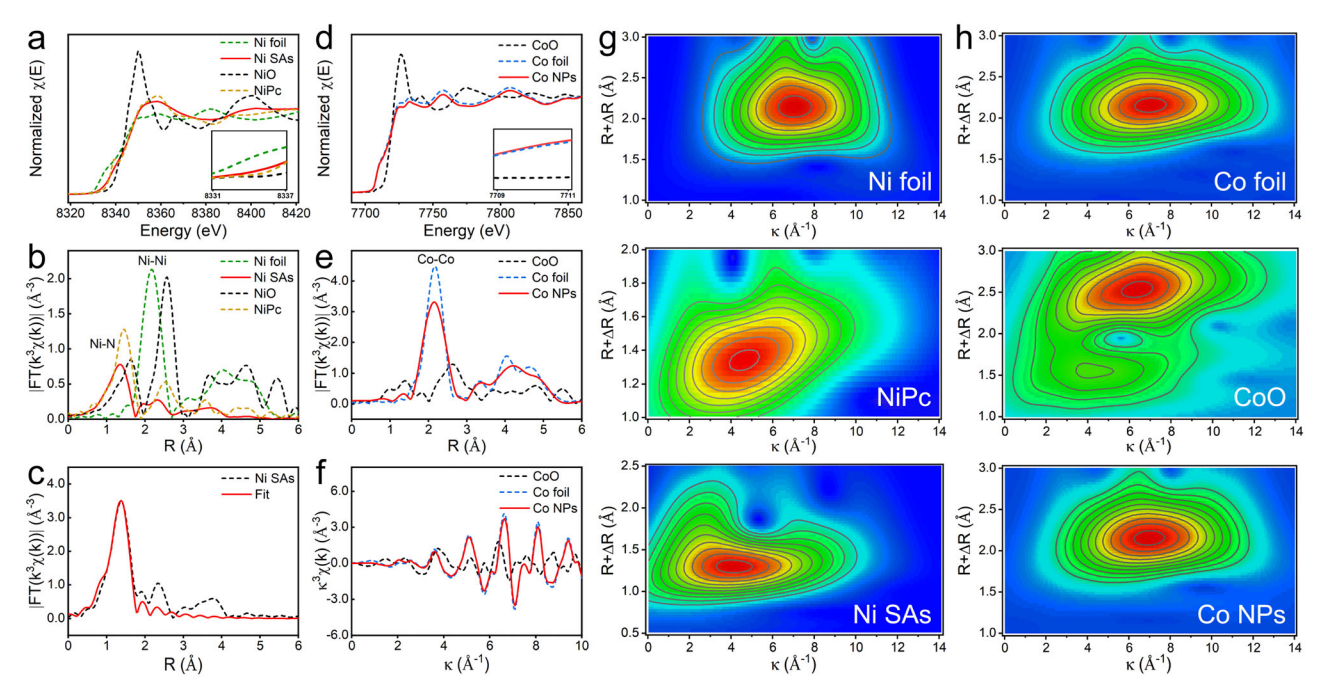


Fig. 3 | **XAFS analysis for dual-active-site catalyst Ni SAs-Co NPs. a** Ni K-edge XANES spectra (inset: magnified absorption edges) and \mathbf{b} $\chi(R)$ spectra of Ni SAs, NiO, NiPc and Ni foil. \mathbf{c} EXAFS *R*-space fitting results of Ni SAs. \mathbf{d} Co K-edge XANES spectra (Inset: magnified absorption edges), \mathbf{e} , $\mathbf{f}\chi(R)$ spectra and the corresponding

EXAFS k-space of Ni SAs-Co NPs, CoO, and Co foil. **g**, **h** Wavelet transform of $\chi(k)$ of Ni and Co for and other reference samples. Source data are provided as a Source Data file.

The detailed parameters of local atomic structure, including coordination numbers and bond lengths were investigated via extended X-ray absorption fine structure (EXAFS). The radial distance space spectra $\chi(R)$ for the Ni SAs and NiPc show a major peak at 1.44 Å, which is attributed to the Ni-N scattering path. The peak at 2.18 Å for Ni foil could be assigned to the Ni-Ni scattering path (Fig. 3b). No Ni-Ni signals could be found for both Ni SAs and NiPc³⁶. The quantitative $\chi(R)$ and $\chi(k)$ space spectral fitting was also performed to investigate local atomic structure and to further obtain the coordination numbers (CNs) of Ni. The CN of Ni-N bond is close to 3.0 for NiN₃ SAs (Supplementary Table 3). The fitting quantitative $\chi(R)$ space and Fourier transform (FT) k^2 -weighted function $\chi(k)$ spectra were also performed from Fig. 3c, d and Supplementary Fig. 8. The results indicate that the Ni is single-atomically dispersed on CNTs. Figure 3d shows that the prepared Ni SAs-Co NPs displays a XANES profile similar to that of Co foil, indicating the formation of Co NPs. As shown in Fig. 3e, the EXAFS shows a major peak at 2.12 Å, which can be assigned to the Co-Co shells by comparing with Co foil²⁸. The quantitative $\chi(k)$ space spectra were also fitted (Fig. 3f). In addition, the wavelet transform (WT) of $\chi(k)$ is an intuitive way to demonstrate the bonding features of Ni SAs-Co NPs in comparison to the reference samples (Fig. 2g, h). For the Ni WT of $\chi(k)$ spectra of Ni, the characteristic signal of the Ni-Ni scattering path in Ni foil is at [7.1, 2.2]. There is only one merged scattering path signal ascribed to Ni-N located at $[\chi(k), \chi(R)]$ of [4.0, 1.4], which is similar to that of NiPc. For the Co WT of $\chi(k)$ spectra of Co, compared with the characteristic scattering path signal of Co-Co bond in Co foil (at [7.3, 2.2]) and Co-O bond in CoO (at [6.2, 2.6]), the single scattering path signal is similar to that for Co foil, indicative of Co-Co bond in Ni SAs-Co NPs. Compared with Ni SACs, the Co catalyst exists in the form of nanoparticles in the dual-active-site catalyst.

The elemental composition and valence states were analyzed via X-ray photoelectron spectroscopy (XPS). As shown in Supplementary Fig. 9, the survey spectra reveal the existence of the corresponding elements in different samples, including Ni SAs–Co NPs, Ni SAs, and Co NPs. For dual-active-site catalyst Ni SAs–Co NPs, it can be noted that the surface of the samples contains C, N, Co, and Ni elements. For Co

2p XPS spectra for Ni SAs–Co NPs s, the binding energies at 778.5 eV and 794.3 eV are attributed to the metal Co⁰, and the peaks at 797.0 and 781.6 eV are attributed to Co²⁺, accompanied by two satellite peaks (786.5 and 803.94 eV, respectively)³⁷. The sample surfaces might be oxidized owing to exposure to air during handling. In addition, as shown in Raman spectra (Supplementary Fig. 10), the D peak (1345 cm⁻¹) is due to out-of-plane vibrations attributed to the presence of structural defects, whereas the G peak (1580 cm⁻¹) comes from the in-plane vibrations of sp^2 bonded carbon atoms^{38,39}. The I_D/I_G ratio of Ni SAs has the highest value, indicative of more defects owing to the lower coordination numbers (3.0). The I_D/I_G ratio of Ni SAs–Co NPs is between those for Ni SAs and Co NPs.

CO₂RR performances

When photovoltaic panels are to be used as power supply, it is of great importance to ensure that the catalyst during CO₂RR could produce H₂ and CO with an almost constant ratio over a broad potential range. The electrocatalytic CO₂RR performances of our dual-active-site catalyst Ni SAs-Co NPs were evaluated in CO₂-saturated electrolyte using a typical H-type cell with the standard three-electrode setup (Supplementary Fig. 11). As revealed by linear sweep voltammetry (LSV) (Fig. 4a), compared with Co NPs and Ni SAs catalysts⁴⁰, the dual-active sites for Ni SAs-Co NPs catalysts display the highest current density, the lowest onset overpotential and the smallest Tafel slope (Supplementary Fig. 12). Furthermore, the LSV curves for different catalysts were recorded in Ar-saturated electrolytes (inset of Fig. 4a), and the Ni SAs-Co NPs shows a good performance of water electrolysis. The gasphase and liquid-phase products were detected via gas chromatography (GC) and ¹H NMR⁴¹, respectively (Supplementary Figs. 13, 14). CO and H₂ were identified as the only two products of electrolysis. As shown in Fig. 4b, the Ni SAs display a higher FE_{CO}. CO is the major product at the applied potential (Supplementary Fig. 15). In particular, the FE_{CO} is above 90% from -0.7 to -1.1 V (vs. RHE). By contrast, the Co NPs would preferentially produce H₂, and the FE_{H2} is above 80% at the applied potential (Supplementary Fig. 16). As shown in Fig. 4c and Supplementary Fig. 17, H2 is the major product over Co NPs at the

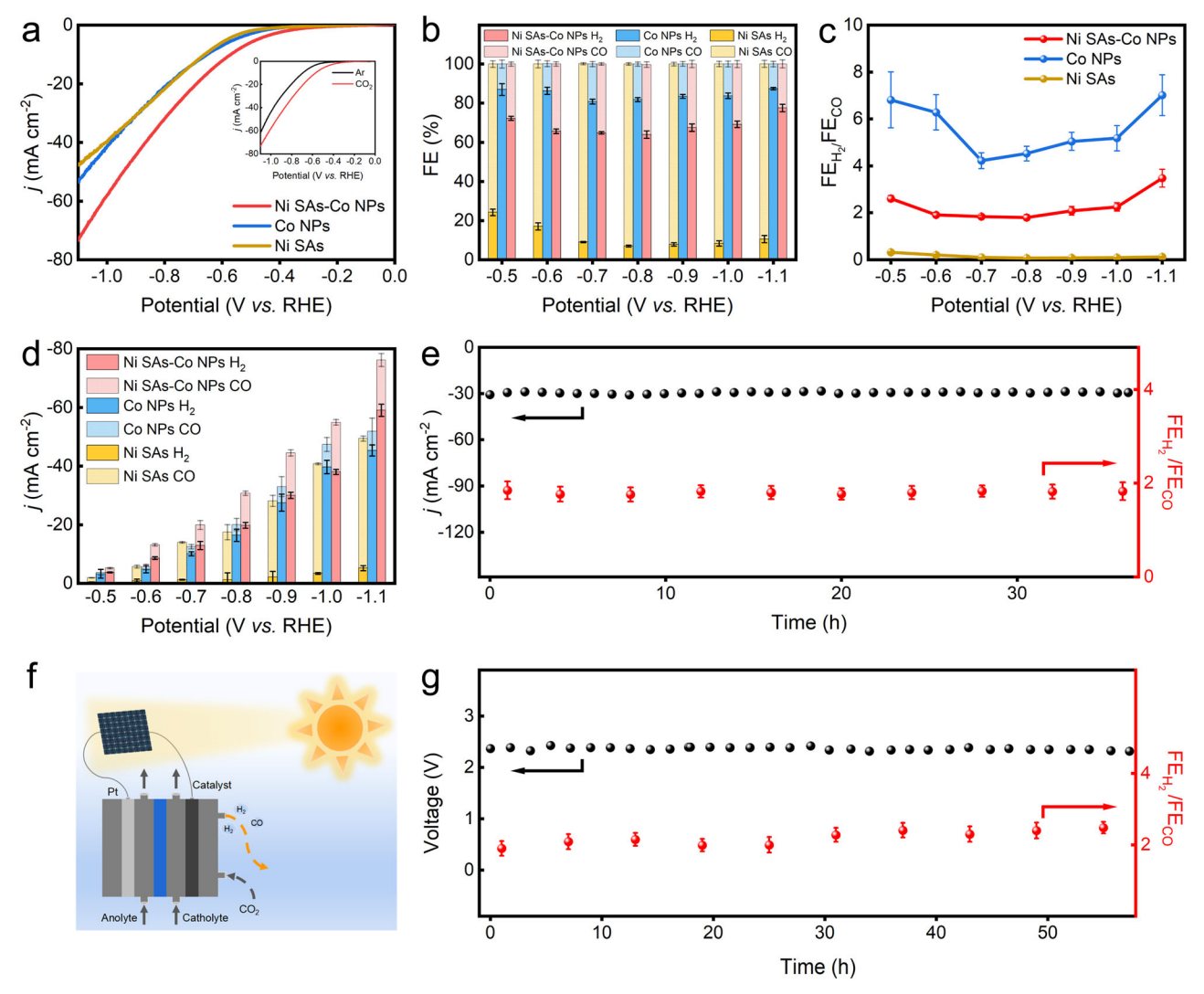


Fig. 4 | **The performance for CO₂RR. a** LSV (Potentials are non-iR-corrected; Scan rate: 5 mV s⁻¹; Inset, LSV of dual-active-site catalyst Ni SAs-Co NP in Ar-saturated 0.5 M KHCO₃). **b** FE_{CO} and FE_{H2}, **c** H₂:CO ratio of syngas and **d** distribution of current density for Ni SAs, Co NPs and Ni SAs-Co NPs catalysts in the CO₂-saturated electrolyte (Potentials are non-iR-corrected). **e** i-t stability of the Ni SAs-Co NPs at

-0.8~V (vs. RHE) and the corresponding H_2 :CO ratio of syngas (Potentials are non-iR-corrected). f Schematic diagram and ${\bf g}$ stability of the flow cell when powered by a photovoltaic panel. Error bars represent the standard deviation derived from three independent measurements. Source data are provided as a Source Data file.

applied potential, and the primary product over Ni SAs is CO. We furthermore prepared comparison catalysts with different amounts of Ni species introduced. It can be seen that a lower Ni ratio would lead to a higher H_2 :CO ratio (Supplementary Fig. 18). Thus, the H_2 :CO ratio in syngas could be precisely controlled by regulating the ratio of the two active sites (single-atomic sites and nanocrystals). The H_2 :CO ratio over-optimized Ni SAs–Co NPs was adjusted and kept around 2.0 over the broad potential from -0.6 to -1.0 V (vs. RHE).

Figure 4d shows the partial current densities for different catalysts, in which the current density for Ni SAs–Co NPs is 30.5 mA cm $^{-2}$ at $-0.8\,V$ (vs. RHE). The current density for Ni SAs–Co NPs increases acutely with increased applied potential and reaches up to 76.1 mA cm $^{-2}$ at $-1.1\,V$ (vs. RHE). Moreover, the long-term stability and corresponding H_2 :CO ratio were assessed for Ni SAs–Co NPs, which exhibit outstanding stability for CO₂RR, with the H_2 :CO ratio kept around 2.0 ± 0.2 and the current density unchanged at $^{-3}0.0\,\text{mA}\,\text{cm}^{-2}$ during continuous electrolysis for 36 h (Fig. 4e). Furthermore, the different catalyst loadings were tested in both H-type cell and flow cell (Supplementary Fig. 19). As shown in Fig. 4f, a solar cell was used as the photovoltaic power source, and the Ni SAs–Co NPs was tested in flow cell configuration (Supplementary Fig. 20). The current density

reached up to $60.0\,\text{mA}\,\text{cm}^{-2}$ with the FE $_{\text{H2}}$ and FE $_{\text{CO}}$ almost constant, indicating a stable H $_2$:CO ratio (2.3 ± 0.3). The catalyst displayed good stability (Fig. 4g). The syngas thus produced could be purified and then fed into the downstream photothermal reactor to obtain high-purity CH $_3$ OH.

In order to unveil the structural information during CO_2RR , operando XAFS spectra of the catalysts at Ni and Ni K-edge were recorded. The Operando XAFS spectroscopy was conducted using a customized two-compartment H-type electrochemical cell (Supplementary Fig. 21). The absorption edges in both catalysts shifted slightly to lower energy at more negative potentials, and were basically recovered after the applied potential was removed (Supplementary Figs. 22, 23), indicating that the catalyst structure was stable during CO_2RR . Furthermore, the crystal structure and morphology of catalysts after the CO_2RR test were reexamined via XRD and HRTEM images (Supplementary Figs. 24, 25). The result confirmed that the structure of dual-active-site catalyst Ni SAs–Co NPs is stable during the CO_2RR process^{42–45}.

Theoretical analysis

Density functional theory (DFT) calculations were performed to gain insight into the reaction mechanisms for the dual-active-site catalyst Ni

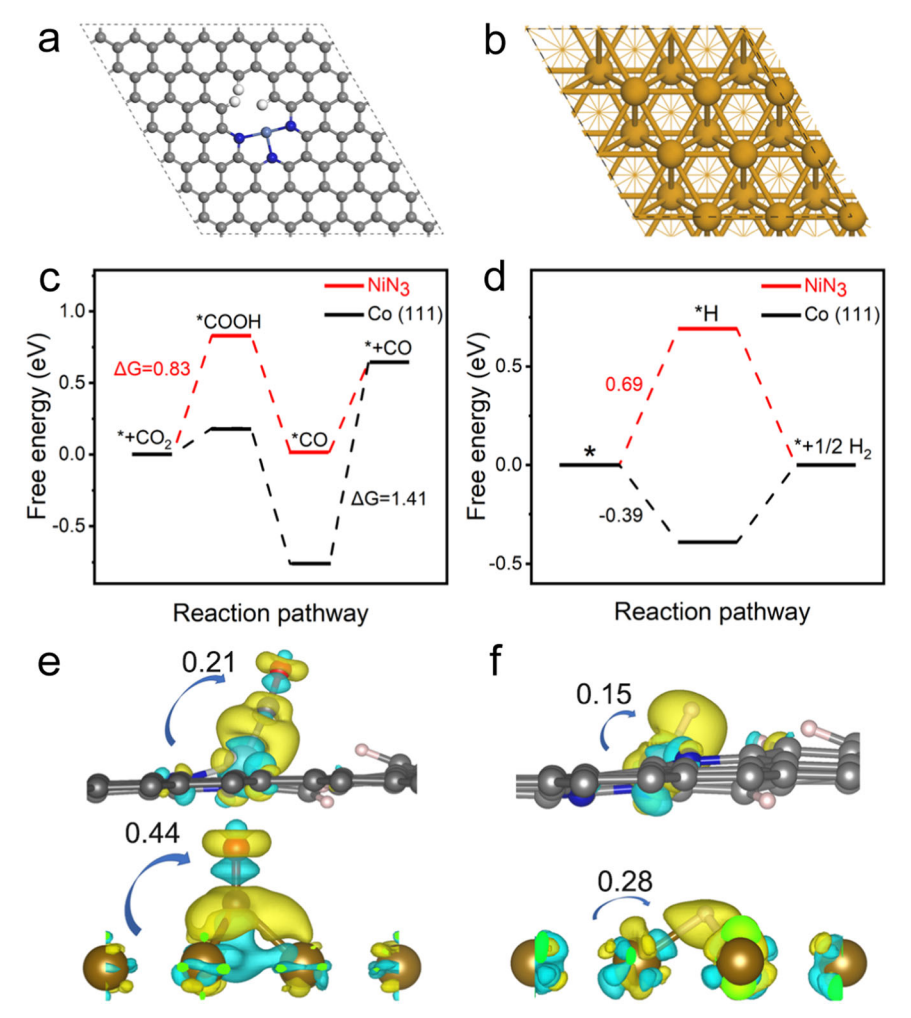


Fig. 5 | Theoretical calculations on dual-active-site catalyst Ni SAs-Co NPs. a, b Calculation models constructed for NiN $_3$ and Co(111) (top view) (The light-blue, blue, gray, gold, and white spheres represent Ni, N, C, Co, and H atoms, respectively.). c, d Free energy diagrams for NiN $_3$ and Co(111) for CO $_2$ RR and HER. e, f The

charge density difference of adsorbed CO and H on NiN $_3$ or Co(111) with an isosurface level of 0.004 e Å $^{-3}$. Yellow represents charge accumulation, and cyan represents charge depletion.

SAs-Co NPs. Models of NiN₃ (Fig. 5a) and Co(111) catalytic surfaces (Fig. 5b) were constructed to represent the Ni SAs and Co NPs in the catalyst, respectively (for further details, see Supplementary Information and Supplementary Data 1). The free energy diagrams of CO₂ reduction into CO were computed and depicted in Fig. 5c, revealing that for the potential-limiting step, NiN3 has a moderate value of 0.83 eV. In contrast, for the Co(111) surface, a large energy (1.41 eV) input is required for CO desorption. The H adsorption free energy $\Delta G_{\rm H}$ was also calculated⁴⁶. Figure 5d shows that the Co(111) surface has a $\Delta G_{\rm H}$ value similar to that of the Pt(111) surface reported⁴¹, whereas NiN₃ has a rather high $\Delta G_{\rm H}$ value (0.69 eV), indicating a poor ability to produce H₂. The difference in carbon species adsorption can be explained by both the charge density difference and Bader charge analysis on CO adsorbed Co(111) and NiN3 models. In the former model, the CO gains more negative charge than in the latter one (0.44 e vs. 0.21 e), as shown in Fig. 5e. Interestingly, similar to the adsorption of CO molecules, the adsorption of H on Co(111) leads to gaining more negative charge (0.28 e), thus stabilizing the adsorption of H on Co(111) (Fig. 5f). In addition, according to the Butler-Evans-Putterman relationship, for reactions of the same type, the activation energy generally varies linearly with the reaction free energy (ΔG). Therefore, ΔG can serve as the metric to explain the preferences for different active sites. Those results are consistent with experimental findings that single-atomic Ni centers are responsible for CO₂ reduction into CO,

and Co nanoparticles contribute primarily to $\rm H_2$ formation over the Ni SAs–Co NPs catalyst.

Discussion

For the challenging task of converting CO₂ into high-purity CH₃OH using solar energy for sustainable development, we designed a sunlight-driven tandem catalytic system that integrated electrochemical CO2RR and photothermally powered CO hydrogenation, which could produce CH₃OH in high purity (the volume fraction of CH₃OH/(CH₃OH + H₂O) ranging from 97 to 100%). For the electrocatalytic CO₂RR, an in situ synthesis strategy was developed to prepare a self-supporting binary catalyst with dual-active sites. The single-atomic NiN3 sites were anchored on the surface during the growth of carbon nanotubes encapsulating Co nanoparticles. The detailed parameters of local atomic structures, including coordination numbers and bond lengths for electrocatalyst dual-active sites were further analyzed via XAFS spectroscopy. For CO₂RR performance, the NiN₃ SAs displayed a high FE_{CO}, and the Co NPs would preferentially produce H₂. The optimized electrocatalyst could produce syngas with a constant H₂:CO molar ratio of around 2:1 over a broad potential window. The produced syngas, after purification, could be further fed into the downstream photothermal reactor powered by broad-spectrum solar irradiation. The CH₃OH production rate under 1 sun was 238 mg g_{cat}⁻¹ h⁻¹. Our work here demonstrates a sun-simulated-driven route to converting CO₂ into high-purity

CH₃OH via the coupling of photovoltaics-powered electrocatalysis and photothermal catalysis. This approach makes the solar-driven production of high-concentration CH₃OH a reality.

Methods

Materials

All the chemical reagents were purchased from commercial sources and used directly without further purification. Cobalt nitrate hexahydrate (Co(NO₃)₂ 6H₂O, Hebei Bailingwei Superfine Materials Co., Ltd., 99%), 2-methylimidazole(Hebei Bailingwei Superfine Materials Co., Ltd., 99%), cyanuric acid (CA, Sahn Chemical Technology (Shanghai) Co., Ltd., 99%), 2,4-diamino-6-phenyl-1,3,5-triazine (DPT, Sahn Chemical Technology (Shanghai) Co., Ltd., 99%), nickel chloride hexahydrate(NiCl₂ 6H₂O, Shanghai Aladdin Biochemical Technology Co., Ltd., 98%), potassium bicarbonate (KHCO₃, Shanghai Aladdin Biochemical Technology Co., Ltd., 99.5%), CuZnAlO_x (SCST-253, purchased from Sichuan Shutai Chemical Technology Co., Ltd), melamine (Shanghai Titan Technology Co., Ltd., 99%), ethanol (EtOH, Tianjin FuChen Chemical Reagent Co., Ltd., 99.7%), methanol (MeOH, Tianjin FuChen Chemical Reagent Co., Ltd., 99.7%), carbon dioxide gas (CO₂, 99.999%), argon gas (Ar, 99.999%), and nitrogen gas (N₂, 99.999%) were purchased from Tianjin Huanyu Gas Co., Ltd., Nafion solution (Sigma-Aldrich, 5 wt%), proton exchange membrane (Nafion 117, thickness: 183 µm, Dupont), Ag/AgCl reference electrode and Pt wire electrode were obtained from Gaoss Union. Carbon paper (SigracetGDL29BC) was purchased from FuelCellsEtc. Ultra-pure water (resistance >18.2 M Ω cm) was used in all experimental processes.

Synthesis procedures

In situ preparation procedure for the dual-active-site catalyst. The prepared ZIF-67 $(0.30\,\mathrm{g})$ and melamine $(0.90\,\mathrm{g})$ were both dispersed in ethanol and ultrasonicated for 30 min, washed three times with ethanol, and dried in vacuum at $60\,^{\circ}\mathrm{C}$ for 6 h. Cyanuric acid (CA, 6.0 mmol), 2,4-diamino-6-phenyl-1,3,5-triazine (DPT, 6 mmol), and Ni(NO₃)₂-6H₂O $(0.18\,\mathrm{mmol})$ were added to ultra-pure water $(40.0\,\mathrm{mL})$, stirred violently at room temperature for 6 h, centrifuged with ultra-pure water, and the powder was dried in vacuum at $60\,^{\circ}\mathrm{C}$ for 24 h.

The two powders were fully ground and mixed in a mortar and transferred to a porcelain boat, and then put into a tube furnace to carry out stage-by-stage high-temperature pyrolysis in N₂ atmosphere: heating up to 550 °C at a ramping rate of 2.3 °C min⁻¹ for 2 h, then heating up to 800 °C at a ramping rate of 10 °C min⁻¹ for 1 h, and finally natural cooling to obtain a fluffy carbon nanotube structure, namely, Ni SAs–Co NPs.

Synthesis of ZIF-67. 2-methylimidazole (0.20 mol) was dissolved in methanol (500.0 mL), and $Co(NO_3)_2\cdot 6H_2O$ (0.05 mol M) was dissolved in methanol (500.0 mL). And then, the solution of 2-methylimidazole was poured into the solution of $Co(NO_3)_2\cdot 6H_2O$. The mixture was stirred at room temperature for 24 h, washed three times with methanol, and dried in vacuum at 60 °C for 12 h. ZIF-67 powder was thus obtained.

Synthesis of Co NPs. The prepared ZIF-67 (0.30 g) and melamine (0.90 g) were both dispersed in ethanol and ultrasonicated for 30 min, washed three times by ethanol, and dried in vacuum at 60 °C for 6 h. After fully ground in a mortar, the powder was transferred to a porcelain boat and put into a tube furnace to carry out stage-by-stage high-temperature pyrolysis in an N_2 atmosphere: heating up to 550 °C at a ramping rate of 2.3 °C min⁻¹ for 2 h, then heating up to 800 °C at a ramping rate of 10 °C min⁻¹ for 1 h, and finally cooling to obtain fluffy carbon nanotubes with core-shell structure, namely, Co NCs.

Synthesis of Ni SAs. The Ni SAs was prepared by a previously reported method. Cyanuric acid (CA, 6.0 mmol), 2,4-diamino-6-phenyl-1,3,5-

triazine (DPT, 6.0 mmol), and Ni(NO₃)₂·6H₂O (0.18 mmol) were added to ultra-pure water (40.0 mL), stirred violently at room temperature for 6 h, centrifuged with ultra-pure water, and the powder was dried in vacuum at 60 °C for 24 h. After fully ground in a mortar, it was transferred to a porcelain boat and put into a tube furnace to carry out stage-by-stage high-temperature pyrolysis in an N₂ atmosphere: heating up to 550 °C at a ramping rate of 2.3 °C min⁻¹ for 2 h, then heating up to 800 °C at a ramping rate of 10 °C min⁻¹ for 1 h, and finally natural cooling to get a black solid, which was fully ground to a black powder, namely, Ni SAs.

Characterizations

The X-ray diffraction (XRD) test was carried out on a SmartLab 9 kW X-ray diffractometer (Rigaku). The instrument was equipped with a Cu-Kα radiation ($\lambda = 1.5418 \text{ Å}$), working voltage 40 kV, working current 150 mA, in the range of 2θ from 20° to 80° with a scan rate of 10° min⁻¹. Scanning electron microscopy (SEM) images were collected with a Quanta FEG 250 environment scanning electron microscope with a field emission gun produced by FEI Company. Transmission electron microscopy (TEM) was performed on a LaB₆ transmission electron microscope of TECNAI G2 Spirit TWIN produced by FEI Company, and the acceleration voltage was 120 kV. High-resolution transmission electron microscopy (HRTEM) was conducted on a Talos F200 X microscope produced by the FEI company. The electron beam energy range was 0.1-8 keV, and the acceleration voltage was 120 kV. High-angle annular dark-field scanning TEM (HAADF-STEM) was conducted on a Titan Cubed Themis G2 300 produced by FEI company. Elemental analysis was carried out via iCAP RQ inductively coupled plasma optical emission spectroscopy (ICP-MS) produced by Semel Fisher Technology Co., Ltd., Germany. X-ray photoelectron spectroscopy (XPS) was conducted on an ESCALAB250Xi type X-ray photoelectron spectrometer with Al Kα as the excitation source produced by Thermo Scientific.

Electrochemical measurements

The performance for electrochemical CO₂ reduction was assessed on an electrochemical workstation (CHI 760E) produced by Shanghai Chenhua Instrument Co., Ltd. The electrolyte was prepared and used immediately when needed. The test was carried out in an H-type electrolytic cell. The cathode and anode in the cell were separated by a proton exchange membrane (Nafion 117), and a certain amount of KHCO₃ (0.5 M, pH = 7.3 ± 0.05) was added as the electrolyte. The electrolyte volume used in both cathodic and anodic chambers was 17 mL. A platinum plate $(1 \times 1 \text{ cm}^2)$ was used as a counter electrode, Ag/ AgCl as the reference electrode, and carbon paper $(0.5 \times 2.0 \text{ cm}^2)$ coated with the catalyst as a working electrode. The Ag/AgCl reference electrode was calibrated using a reversible hydrogen electrode (RHE) under controlled conditions. The calibration was carried out in a highpurity H₂-saturated electrolyte (0.5 M H₂SO₄) with a Pt wire as the working electrode, a graphite rod as the counter electrode, and the Ag/ AgCl electrode as the reference. Cyclic voltammetry was run at a scan rate of 1 mV s⁻¹, and the average of the two potentials at which the current crossed zero was taken to be the thermodynamic potential for the hydrogen electrode reactions.

Pretreatment of Nafion 117 membrane. First, the proton exchange membrane (Nafion 117) was soaked in hydrogen peroxide solution (5%) at $80\,^{\circ}\text{C}$ for 1 h, then in deionized water for $0.5\,\text{h}$. Then it was soaked in H_2SO_4 solution (mass ratio 5%) at $80\,^{\circ}\text{C}$ for 1 h, and finally soaked in deionized water for $0.5\,\text{h}$.

The preparation of the working electrode used the method of drop casting: the sample (3.0 mg) was dispersed into 50 μ L Nafion and 550 μ L ethanol mixed solution, ultrasonicated for 30 min to form a uniform ink, and then 300-uL ink was evenly dispensed onto 0.5 × 2 cm⁻² carbon paper, and dried naturally The catalyst loading was 1.5 mg cm⁻². The potentials used in this paper were converted with

respect to reversible hydrogen electrode:

$$E(RHE) = E(Ag/AgCl) + 0.0592 \times pH + 0.197$$
 (1)

In this experiment, the gas-phase products were determined both qualitatively and quantitatively on a Shimadzu GC-2014 gas chromatograph, which was equipped with thermal conductivity detectors and flame ionization detectors. High-purity argon was used as the carrier gas (99.999%). Ethane, ethylene, methane, carbon monoxide, hydrogen, and oxygen could be detected at the same time, and the gas-phase products could be determined by the external standard method. The Faradaic efficiencies of the gas-phase products were calculated according to the following equations:

$$FE = \frac{n \times z \times F}{Q} \times 100\% \tag{2}$$

FE: Faradaic efficiency for H₂ or CO production;

n: The molarity of the product, mol;

z: The number of electrons transferred during the electrocatalytic process (2 here);

F: Faraday constant (96485 C/mol);

Q: the input charge (C).

CO and H_2 partial current densities (j_{CO}) can be obtained according to the following equation:

$$j_{CO/H2} = \frac{FE_{CO/H2} \cdot I}{S}$$
 (3)

where *I* is the average current, and *S* represents the geometric surface area of the working electrode.

The liquid-phase products in CO_2RR were quantitatively analyzed via 1H NMR spectroscopy (AVANCE III HD 400 MHz, Brooke Company in Switzerland). The LSV curves were recorded in CO_2 -saturated and Ar-saturated 0.5 M KHCO $_3$ solutions with the scan rate of 5 mV s $^{-1}$ in the H-cell system.

Flow cell tests. The electrochemical measurements were conducted in a three-channel flow cell. The catalyst was coated onto a carbon paper with a mass loading of 3.0 mg cm $^{-2}$. Pt was used as the counter electrode, and a leak-free Ag/AgCl as the reference electrode. The electrolyte was 0.5 M KHCO $_3$. In the flow cell, the proton exchange membrane (Nafion 117) was used as the separator placed between the anode/cathode compartments. The membrane facilitates ion transport while minimizing product crossover. Each compartment has a serpentine flow channel. On the cathode side, CO $_2$ flew through the channel over the surface of carbon paper coated with the catalyst, producing CO and H $_2$; on the anode side, the electrolyte flew through the channel and produced O $_2$ over the anode catalyst. The CO $_2$ gas flow rate was set to be 15 sccm and the flow rate of electrolyte was 20 mL min $^{-1}$ via a peristaltic pump. The solar cell was purchased from commercial sources and used as power for CO $_2$ RR.

Operando XAFS measurements. The *Operando* XAFS spectroscopy was conducted using a customized two-compartment H-type electrochemical cell. The schematic of the cell could be found in Supplementary Fig. 20. The cell is comprised of the working, counter (Pt wire), and references electrodes (Ag/AgCl), inlets and outlets. The high-purity CO_2 (99.999%) was fed during the test. The prepared catalyst ink was dispensed on a carbon paper (SigracetGDL29BC) electrode and dried. A small window was cut out on the cathode side and sealed with Kapton film to allow the fluorescence signals to pass from the electrode to the detector. To record the operando XANES spectra, the cell was subsequently filled with electrolyte (0.5 M KHCO₃ aqueous solution), and bubbled with CO_2 for 30 min before test. The *operando* XANES spectra were recorded under open-circuit potential (OCP), and

then recorded under different applied potentials. The applied potential was controlled by the electrochemical workstation (CHI 760E). The measures were conducted at room temperature.

Photothermal performance. The photothermal methanol synthesis was tested as follows: 20 mg of commercial CuZnAlO_x (SCST-253. purchased from Sichuan Shutai Chemical Technology Co., Ltd) was placed into the TiC/Cu-based photothermal device and irradiated by a light source (DL-3000). The CO and H₂ generated by photovoltaic electrocatalysis were first pressurized to 4 MPa through a pressurization device and then introduced into the photothermal device with a flow rate of 0.5 mL min⁻¹. The reaction products were tested by gas chromatography (GC) 7890A equipped with FID and TCD detectors. For the purification of green syngas, we used KOH aqueous solution (2 M) to remove the excess CO₂ and then used 3A molecular sieves to remove residual water. The column used for testing methanol was a capillary chromatography column (LZP-950). We used the method of injection to detect the signal of methanol. The gas coming out of the outlet was kept in a tube (kept at 120 °C, so that methanol would exist as vapor), and we used a syringe to quantitatively extract the gas, and then injected it into the gas chromatograph (GC), so that all substances would be detected.

The preparation of photothermal device. The reaction tube was 45 cm in length and 4 cm in diameter. Then, the SP-0707AS magnetron sputtering was used to deposit Cu film and TiC film, which had a 4-axis rotation system to rotate bases. Cu and TiC were used as targets; the working gas was Ar (99.99% purity). Before the deposition process, the tube was washed with deionized water, acetone, and ethanol. The deposition of Cu substrate and TiC film on the reaction tube first used glow-discharge to clean the stainless tube, and then the Cu layer and the TiC film were deposited sequentially, and the sample was taken out after passive cooling. Specific parameters: the power was 5 KW, the sputtering pressure was 9×10^{-2} Pa, the bias voltage was 150 V, the sputtering temperature was 70 °C, the sputtering durations for Cu layer and TiC film were 25 and 6 min, respectively. The glass vacuum layer had a pressure of 1×10^{-3} Pa.

Finite-element analysis. COMSOL Multiphysics 6.1 was used to conduct the finite-element analysis on the photothermal tube. The modules of "Laminar flow", "Heat transfer in fluids" and "Transport of concentrated species" were employed. The photothermal tube was set to have a diameter of 45 mm and a length of 450 mm. At the inlet, a flow rate of 24 sccm, a temperature of 293 K, and a CO:H₂:CH₃OH molar ratio of 1:2:0 were set; at the outlet, an absolute pressure of 1 atm was set. At the side wall of the photothermal tube, a temperature of 593 K was set. The thermocatalytic CO hydrogenation reaction was assumed to be irreversible and have a reaction order of 1 with respect to CO, and 2 with respect to H₂. The heat generation for each mole of generated CH₃OH was set to be 90.5 kJ. The rate constant k was swept to ensure an overall CH₃OH production rate of 0.238 g h⁻¹ (as determined experimentally).

Computational details. In this work, all the first-principles calculations were performed by using the Vienna ab initio simulation package (VASP) (*Phys. Rev. B* **54**, 11169–11186 (1996)) based on the spin-polarized density functional theory (DFT). The generalized gradient approximation (GGA) within the Perdew–Burke–Ernzerhof (PBE) (*Phys. Rev. Lett.* **77**, 3865–3868 (1996)) functional was used to describe the exchange-correlation energy. The projector augmented-wave (PAW) method (*Phys. Rev. B* **50**, 17953–17979 (1994)) with a plane-wave basis set with an energy cut-off of 450 eV was used for total energy calculations. In order to account for van der Waals interactions, the DFT-D3 method with Becke-Jonson damping was employed (*J. Chem. Phys.* **132**, 154104 (2010); *Energy Environ. Sci.* **3**, 1311–1315 (2010). The

convergence criterion of energy and force was set to $10^{-5}\,\text{eV}$ and $0.02\,\text{eV}\,\text{Å}^{-1}$, respectively.

To investigate the effect of a single nickel counterpart of the catalyst, the model of NiN $_3$ was built based on a N-doped graphene in a $7 \times 7 \times 1$ supercell. Additionally, the unsaturated carbon was passivated by pseudo-hydrogen to saturate dangling bonds. A vacuum layer of 20 Å was incorporated to prevent interaction between layers. Co nanoparticles were modeled using the Co(111) surface according to the experimental observation. This surface was investigated using the periodic $p(3 \times 3)$ supercell and included four atomic layers. During geometry optimizations, the two uppermost layers of the surface were fully relaxed, while the bottom two layers were fixed at their bulk positions. A vacuum layer of 18 Å was added in the direction perpendicular to the surface to avoid interaction with periodically repeated images. Finally, the first Brillouin zone was sampled using a $1 \times 1 \times 1$ and $3 \times 3 \times 1$ Γ -centered k-point grid for NiN $_3$ and Co(111) calculations, respectively.

The reaction pathway for the electrochemical reduction of CO₂ into CO and hydrogen evolution reaction includes the following steps:

$$CO_2 + ^* \rightarrow ^*CO_2$$
 $^*CO_2 + H^+ + e^- \rightarrow ^*COOH$
 $^*COOH + H^+ + e^- \rightarrow ^*CO + H_2O$
 $^*CO \rightarrow CO + ^*$
 $^*H^+ + e^- \rightarrow ^*H$
 $^*H + H^+ + e^- \rightarrow 1/2H_2$

The change in Gibbs free energy of each reaction pathway is defined by:

$$\triangle G = \triangle E + \triangle ZPE - T \triangle S \tag{4}$$

where ΔE is the energy difference based on DFT calculations, ΔZPE and ΔS (Table S3) are the zero-point energy (ZPE) correction and the entropy change, respectively, T represents the temperature and set to be 298.15 K.

The adsorption energy was calculated by:

$$E_{\text{ads}} = E_{\text{total}} - (E_{\text{substrate}} + E_{\text{adsorbate}})$$
 (5)

where $E_{\rm total}$, $E_{\rm slab}$, and $E_{\rm adsorbate}$ are the total energy of substrate with adsorbate, the substrate, and the isolated adsorbate, respectively. The more negative adsorption energy corresponds to stronger adsorption.

Data availability

All data were available in the main text or the Supplementary Information. Atomic coordinates of the optimized models are provided in Supplementary Data. Source data are provided with this paper.

References

- Li, P. et al. In situ dual doping for constructing efficient CO₂-tomethanol electrocatalysts. Nat. Commun. 13, 1965 (2022).
- Wang, J. et al. A highly selective and stable ZnO-ZrO₂ solid solution catalyst for CO₂ hydrogenation to methanol. Sci. Adv. 3, e1701290 (2017).
- 3. Liang, J. M. et al. CO_2 hydrogenation over Fe-Co bimetallic catalysts with tunable selectivity through a graphene fencing approach. *Nat. Commun.* **15**, 512 (2024).

- Pan, X., Jiao, F., Miao, D. & Bao, X. Oxide-zeolite-based composite catalyst concept that enables syngas chemistry beyond fischertropsch synthesis. Chem. Rev. 121, 6588–6609 (2021).
- Zhu, P. & Wang, H. High-purity and high-concentration liquid fuels through CO₂ electroreduction. *Nat. Catal.* 4, 943–951 (2021)
- Li, J., Guo, J. & Dai, H. Probing dissolved CO₂(aq) in aqueous solutions for CO₂ electroreduction and storage. Sci. Adv. 8, eabo0399 (2022).
- Wang, B., Chen, S., Zhang, Z. & Wang, D. Low-dimensional material supported single-atom catalysts for electrochemical CO₂ reduction. SmartMat 3, 84–110 (2022).
- Wei, W., Kong, Y., Xu, L. & Chen, C. Electrochemical synthesis of organonitrogen compounds from N-integrated CO₂ reduction reaction. Acta Phys. Chim. Sin. 40, 2307049 (2023).
- Wang, Y., Zheng, X. & Wang, D. Design concept for electrocatalysts. Nano Res. 15, 1730–1752 (2022).
- Tackett, B. M., Gomez, E. & Chen, J. G. Net reduction of CO₂ via its thermocatalytic and electrocatalytic transformation reactions in standard and hybrid processes. *Nat. Catal.* 2, 381–386 (2019).
- Yang, H. et al. Scalable production of efficient single-atom copper decorated carbon membranes for CO₂ electroreduction to methanol. J. Am. Chem. Soc. 141, 12717–12723 (2019).
- 12. Kuhl, K. P. et al. Electrocatalytic conversion of carbon dioxide to methane and methanol on transition metal surfaces. *J. Am. Chem.* Soc. **136**, 14107–14113 (2014).
- Navarro-Jaén, S. et al. Highlights and challenges in the selective reduction of carbon dioxide to methanol. *Nat. Rev. Chem.* 5, 564–579 (2021).
- Kong, S. et al. Delocalization state-induced selective bond breaking for efficient methanol electrosynthesis from CO₂. Nat. Catal. 6, 6–15 (2023).
- Lu, L. et al. Highly efficient electroreduction of CO₂ to methanol on palladium-copper bimetallic aerogels. *Angew. Chem. Int. Ed.* 57, 14149–14153 (2018).
- Zhang, G. et al. Selective CO₂ electroreduction to methanol via enhanced oxygen bonding. Nat. Commun. 13, 7768 (2022).
- 17. Wu, Y., Jiang, Z., Lu, X., Liang, Y. & Wang, H. Domino electro-reduction of $\rm CO_2$ to methanol on a molecular catalyst. *Nature* **575**, 639–642 (2019).
- 18. Huang, J., Guo, X., Yue, G., Hu, Q. & Wang, L. Boosting CH_3OH production in electrocatalytic CO_2 reduction over partially oxidized 5 nm cobalt nanoparticles dispersed on single-layer nitrogendoped graphene. ACS Appl. Mater. Interfaces **10**, 44403–44414 (2018).
- Ren, X. et al. In-situ spectroscopic probe of the intrinsic structure feature of single-atom center in electrochemical CO/CO₂ reduction to methanol. *Nat. Commun.* 14, 3401 (2023).
- Das, S. et al. Core-shell structured catalysts for thermocatalytic, photocatalytic, and electrocatalytic conversion of CO₂. Chem. Soc. Rev. 49, 2937–3004 (2020).
- 21. Hu, J. et al. Sulfur vacancy-rich MoS_2 as a catalyst for the hydrogenation of CO_2 to methanol. *Nat. Catal.* **4**, 242–250 (2021).
- 22. Zhang, Z. et al. New black indium oxide–tandem photothermal CO_2 - H_2 methanol selective catalyst. *Nat. Commun.* **13**, 1512 (2022).
- 23. Ning, S. et al. Co^0 - $Co^{\delta+}$ interface double-site-mediated C-C coupling for the photothermal conversion of CO_2 into light olefins. *Angew. Chem. Int. Ed.* **62**, e202302253 (2023).
- Zhao, R., Zhu, Z., Ouyang, T. & Liu, Z. Q. Selective CO₂-to-syngas conversion enabled by bimetallic gold/zinc sites in partially reduced gold/zinc oxide arrays. *Angew. Chem. Int. Ed.* 136, e202313597 (2024).
- He, Q. et al. Electrochemical conversion of CO₂ to syngas with controllable CO/H₂ ratios over Co and Ni single-atom catalysts. Angew. Chem. Int. Ed. 59, 3033–3037 (2020).

- Min, Z. et al. Enhancing CO₂ electroreduction to syngas by active protons of imidazolium ionic liquids: From performance to mechanism. Appl. Catal. B Environ. 326, 122185 (2023).
- Jiao, J. et al. Constructing asymmetric double-atomic sites for synergistic catalysis of electrochemical CO₂ reduction. *Nat. Com*mun. 14, 6164 (2023).
- Cao, T. et al. Atomically dispersed Ni anchored on polymer-derived mesh-like N-doped carbon nanofibers as an efficient CO₂ electrocatalytic reduction catalyst. Nano Res. 15, 3959–3963 (2022).
- Rong, X., Wang, H. J., Lu, X. L., Si, R. & Lu, T. B. Controlled synthesis of a vacancy-defect single-atom catalyst for boosting CO₂ electroreduction. *Angew. Chem. Int. Ed.* **59**, 1961–1965 (2020).
- Jiao, J. et al. Interface engineering of partially phosphidated Co@Co-P@NPCNTs for highly enhanced electrochemical overall water splitting. Small 16, 2002124 (2020).
- Li, Y. et al. Low temperature thermal and solar heating carbon-free hydrogen production from ammonia using nickel single atom catalysts. Adv. Energy Mater. 12, 2202459 (2022).
- Dang, S. et al. Rationally designed indium oxide catalysts for CO₂ hydrogenation to methanol with high activity and selectivity. Sci. Adv. 6, eaaz2060 (2020).
- Xian, J., Cai, K., Liao, P., Wang, S. & Li, G. Upgrading waste NO_x into amino acids via electrocatalysis on Co nanoparticles encapsulated in hollow carbon nanofibers. Sci. China Chem. 67, 1946–1952 (2024).
- 34. Jiao, J. et al. Doping ruthenium into metal matrix for promoted pHuniversal hydrogen evolution. *Adv. Sci.* **9**, 2200010 (2022).
- Ding, X., Zhang, J. & Li, Y. CO electroreduction: What can we learn from its parent reaction, CO₂ electroreduction? eScience 3, 100137 (2023).
- Jiang, Z. et al. Interfacial assembly of binary atomic metal-N_x sites for high-performance energy devices. *Nat. Commun.* 14, 1822 (2023)
- Bao, L. et al. Anionic defects engineering of Co₃O₄ catalyst for toluene oxida-tion. Fuel 314. 122774 (2022).
- Wang, X. et al. Proton capture strategy for enhancing electrochemical CO₂ reduction on atomically dispersed metal-nitrogen active sites. *Angew. Chem. Int. Ed.* 60, 11959–11965 (2021).
- 39. Sun, N. et al. Promoting oxygen reduction reaction by tuning externally doped nitrogen around atomically dispersed iron. *Fund. Res.* https://doi.org/10.1016/j.fmre.2022.07.014 (2022).
- Chen, X. et al. Enhanced hydrogen evolution reaction performance of MoS₂ by dual metal atoms doping. *Int. J. Hydrog. Energy* 47, 23191–23200 (2022).
- 41. Li, J. et al. Selective CO_2 electrolysis to CO using isolated antimony alloyed copper. *Nat. Commun.* **14**, 340 (2023).
- Martini, A. et al. Tracking the evolution of single-atom catalysts for the CO₂ electrocatalytic reduction using operando X-ray absorption spectroscopy and machine learning. J. Am. Chem. Soc. 145, 17351–17366 (2023).
- 43. Bernal, M. et al. CO_2 electroreduction on copper-cobalt nanoparticles: size and composition effect. Nano Energy **53**, 27–36 (2018).
- 44. Song, D. et al. Electrochemical CO2 reduction catalyzed by organic/inorganic hybrids. eScience **3**, 100097 (2023).
- 45. Guzmán, H., Albo, J., Irabien, A., Castellino, M. & Hernández, S. Role of electrochemical cell configuration on the selectivity of CuZnAl-oxide-based electrodes for the continuous CO₂ conversion: aqueous electrolyte vs. catholyte-less configuration. *Discov. Chem. Eng.* 4, 12 (2024).
- Tripkovic, V. et al. Electrochemical CO₂ and CO reduction on metalfunctionalized porphyrin-like graphene. J. Phys. Chem. C. 117, 9187–9195 (2013).

Acknowledgements

The work was financially supported by the National Key R&D Program of China (No. 2022YFA1502902), National Natural Science Foundation of China (No. 52072260, No. 52472236, No. 21931007, No. 21790052, No. U21A20317, and No. 52371220), Tianjin Natural Science Foundation (21JCZXJC00130 and B2021201074), Science and Technology Support Program for Youth Innovation in Universities of Shandong Province (No. 2020KJA012), Natural Science Foundation of Hebei Province (B2023204034, B2022201090), Haihe Laboratory of Sustainable Chemical Transformations, Supercomputing of Anhui University was acknowledged for computational support. We acknowledge the 1W1B beamline of Beijing Synchrotron Radiation Facility (BSRF) Beijing (China) and the BL14W1 and BL11B beamline of Shanghai Synchrotron Radiation Facility (SSRF) Shanghai for providing the beam time.

Author contributions

J.J. and T.L. conceived the project. Y.M., X.H., H.X., and C.C. carried out the syntheses, structural characterizations, and $\mathrm{CO_2RR}$ tests. Y.L. carried out photothermal measurements. A.E. and Q.L. provided theoretical analysis. Z.S., Y.M., and W.L. provided the test and analysis of the XANES and EXAFS. C.Z. and P.C. conducted the finite-element analysis. J.J. and Y.L. analyzed all the data and prepared the manuscript. All the authors participated in preparing the manuscript.

Competing interests

The authors declare no competing interests.

Additional information

Supplementary information The online version contains supplementary material available at https://doi.org/10.1038/s41467-025-56101-8.

Correspondence and requests for materials should be addressed to Jiqing Jiao, Yaguang Li or Tongbu Lu.

Peer review information *Nature Communications* thanks the anonymous reviewer(s) for their contribution to the peer review of this work. A peer review file is available.

Reprints and permissions information is available at http://www.nature.com/reprints

Publisher's note Springer Nature remains neutral with regard to jurisdictional claims in published maps and institutional affiliations.

Open Access This article is licensed under a Creative Commons Attribution-NonCommercial-NoDerivatives 4.0 International License, which permits any non-commercial use, sharing, distribution and reproduction in any medium or format, as long as you give appropriate credit to the original author(s) and the source, provide a link to the Creative Commons licence, and indicate if you modified the licensed material. You do not have permission under this licence to share adapted material derived from this article or parts of it. The images or other third party material in this article are included in the article's Creative Commons licence, unless indicated otherwise in a credit line to the material. If material is not included in the article's Creative Commons licence and your intended use is not permitted by statutory regulation or exceeds the permitted use, you will need to obtain permission directly from the copyright holder. To view a copy of this licence, visit http://creativecommons.org/licenses/by-nc-nd/4.0/.

© The Author(s) 2025